International Journal of Applied Earth Observations and Geoinformation 101 (2021) 102354

Contents lists available at ScienceDirect

International Journal of Applied Earth Observations and Geoinformation

journal homepage: www.elsevier.com/locate/jag

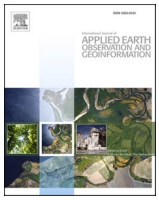

Global fuel moisture content mapping from MODIS

Xingwen Quan [a,b], Marta Yebra [c,d,e,*], David Riaño [f,g], Binbin He [a,*], Gengke Lai [a], Xiangzhuo Liu [h]

[a] School of Resources and Environment, University of Electronic Science and Technology of China, Chengdu, Sichuan 611731, China
[b] Yangtze Delta Region Institute (Huzhou), University of Electronic Science and Technology of China, Huzhou 313001, China
[c] Fenner School of Environment and Society, The Australian National University, ACT, Canberra, Australia
[d] Bushfire & Natural Hazards Cooperative Research Centre, Melbourne, Australia
[e] School of Engineering, The Australian National University, ACT, Canberra, Australia
[f] Center for Spatial Technologies and Remote Sensing (CSTARS), University of California, 139 Veihmeyer Hall, One Shields Avenue, Davis, CA 95616, USA
[g] Instituto de Economía, Geografía y Demografía (IEGD), Centro de Ciencias Humanas y Sociales (CCHS), Consejo Superior de Investigaciones Científicas (CSIC), Albasanz 26-28, 28037 Madrid, Spain
[h] INRAE, UMR1391 ISPA, Université de Bordeaux, F-33140 Villenave d'Ornon, France

ARTICLE INFO

Keywords:
Fire Danger
Fuel Moisture Content
Global Scale
Model Inversion
MODIS
Radiative Transfer Model

ABSTRACT

Fuel moisture content (FMC) of live vegetation is a crucial wildfire risk and spread rate driver. This study presents the first daily FMC product at a global scale and 500 m pixel resolution from the Moderate Resolution Imaging Spectroradiometer (MODIS) and radiative transfer models (RTMs) inversion techniques. Firstly, multisource information parameterized the PROSPECT-5 (leaf level), 4SAIL (grass and shrub canopy level) and GeoSail (tree canopy level) RTMs to generate three look-up tables (LUTs). Each LUT contained the most realistic model inputs range and combination, and the corresponding simulated spectra. Secondly, for each date and location of interest, a global landcover map classified fuels into three classes: grassland, shrubland and forest. For each fuel class, the best LUT-based inversion strategy based on spectral information, cost function, percentage of solutions, and central tendency determined the optimal model for the global FMC product. Finally, 3,034 FMC measurements from 120 worldwide sites validated the statistically significant results ($R^2 = 0.62$, RMSE = 34.57%, $p < 0.01$). Filtering out low quality field measurements achieved better accuracy ($R^2 = 0.71$, RMSE = 32.36%, $p < 0.01$, $n = 2008$). It is anticipated that this global FMC product can assist in wildfire danger modeling, early prediction, suppression and response, as well as improve awareness of wildfire risk to life and property.

1. Introduction

Defined as the proportion of plant water content over its dry mass, Fuel Moisture Content (FMC) of live vegetation is a crucial variable in assessing wildfire risk and fire spread rate (Pimont et al., 2019; Yebra et al., 2013). Developing comprehensive FMC distribution maps worldwide is therefore critical for wildfire early warning and consequent management decisions. Remote sensing can quantitatively infer FMC at an adequate temporal and spatial resolution over large areas. This approach has quickly proliferated over the last two decades using Advanced Very High Resolution Radiometer (AVHRR) (Chladil and Nunez, 1995; Chuvieco et al., 2003; Chuvieco et al., 2004b; Dennison et al., 2008; García et al., 2008; Paltridge and Barber, 1988), Moderate Resolution Imaging Spectroradiometer (MODIS) (Arganaraz et al., 2016; Caccamo et al., 2012; Hao and Qu, 2007; Nolan et al., 2016; Peterson et al., 2008; Yebra and Chuvieco, 2009b; Yebra et al., 2008; Yebra et al., 2018a), Thematic Mapper (TM, Landsat 4, 5), Enhanced Thematic Mapper (ETM+, Landsat 7) and Operational Land Imager (OLI, Landsat 8) (Chuvieco et al., 2002; García et al., 2020; Quan et al., 2016; Quan et al., 2017a), SPOT VEGETATION (Verbesselt et al., 2007), microwave remote sensing (Fan et al., 2018; Leblon et al., 2002; Rao et al., 2020; Tanase et al., 2015; Wang et al., 2019), and airborne hyperspectral data (Al-Moustafa et al., 2012; Casas et al., 2014; Dennison et al., 2003; Neinavaz et al., 2017; Roberts et al., 2006). Among them, MODIS data

* Corresponding authors at: Fenner School of Environment and Society, The Australian National University, ACT, Canberra, Australia (M. Yebra). School of Resources and Environment, University of Electronic Science and Technology of China, Chengdu, Sichuan, China (B. He).
E-mail addresses: marta.yebra@anu.edu.au (M. Yebra), binbinhe@uestc.edu.cn (B. He).

https://doi.org/10.1016/j.jag.2021.102354
Received 23 December 2020; Received in revised form 18 April 2021; Accepted 26 April 2021
Available online 19 May 2021

has attracted more attention to monitoring FMC due to its moderate spatial resolution (250–1,000 m), high temporal resolution, with a morning and an afternoon overpass, long time series since the year 2000, as well as its near-real-time free accessibility.

Methodologies to estimate FMC from remote sensing are broadly classified into empirical statistical models and inversion of radiative transfer models (RTMs) (Yebra et al., 2013). The former techniques set up statistical formulas between field-measured FMC via gravimetric techniques and spectral bands or vegetation indices (VIs) derived from remote sensing images. These formulas are simple and of known accuracy. Therefore, they provide sensor-specific and site-dependent FMC estimations (Yebra et al., 2013). Instead, most RTMs include two input parameters to retrieve FMC (Eq. (1)), the equivalent water thickness (EWT) and dry matter content (DMC) (Riaño et al., 2005),

$$\mathrm{FMC} = \frac{EWT}{DMC} \times 100\% \quad (1)$$

RTMs approaches are more promising as they are built based on physical laws that provide an explicit connection between soil-canopy variables and canopy spectra (Houborg et al., 2007; Meroni et al., 2004; Moorthy et al., 2008). Thus, their advantage is its generalization power to a global scale (Bowyer and Danson, 2004; Yebra et al., 2013; Yebra et al., 2018a). Nevertheless, the accuracy of these RTM-based methods to retrieve biophysical parameters of vegetation rely on (*i*) the proper model selection and parameterization to make the simulated spectra as close as possible to the observed spectra from satellite (Casas et al., 2014; Jurdao et al., 2013; Yebra et al., 2013), and (*ii*) the selection of appropriate inversion strategies to alleviate the ill-posed inversion problem, e.g., different combinations of the model-free parameters may correspond to almost similar spectra, which dramatically decreases the FMC retrieval accuracy (Yebra and Chuvieco, 2009b). In terms of model parameterization, previous studies at a regional scale proved that FMC retrieval from RTM improves when using prior knowledge to constrain the model inputs (Casas et al., 2014; Wang et al., 2013; Yebra and Chuvieco, 2009a, b). Research to validate this model parameterization at the global scale to retrieve FMC is still lacking to date.

The generation of FMC using RTM requires proper model inversion. Current popular inversion algorithms include numerical optimizations (Bicheron and Leroy, 1999; Combal et al., 2003b), look-up tables (LUT) (Quan et al., 2017a; Yebra and Chuvieco, 2009a; Yebra et al., 2008), and machine learning methods (Fang et al., 2003; Quan et al., 2021; Schlerf and Atzberger, 2006). Compared to other algorithms, the LUT is straightforward and computationally efficient to handle large global databases. However, previous studies also revealed different results depending on the inversion strategy, such as the selected spectral information (Jurdao et al., 2013), the chosen cost functions (Verrelst et al., 2013; Verrelst et al., 2015), the number of spectral ensembles to search for a solution (Quan et al., 2017a; Yebra et al., 2018a), and the measurement of central tendency (Darvishzadeh et al., 2008). Consequently, these sources of uncertainties directly affect the estimated FMC accuracy, impacting wildfire prescription and suppression strategies (Chuvieco et al., 2004a; Jolly, 2007; Weise et al., 1998).

Since the 1980 s, remote sensing FMC estimations were well studied mainly for Australia, Spain, France and the USA (Yebra et al., 2013). However, their application was restricted to specific local fire-prone regions, reaching more recently the continental scale (Yebra et al., 2018a). Other fire-prone regions that were historically vulnerable to wildfires, such as the Amazon rain forest region or central Africa, also require studies that estimate FMC from satellite observations. In this context, this study presented the first 500 m spatial resolution and daily satellite-based FMC product at a global scale. The product was generated for a long time series (2001 to 2019) and validated with field data from 120 sites distributed worldwide compiled by Yebra et al. (2019). The overarching objective of the provision of this product is to assist in wildfire danger early prediction, suppression, and response, as well as to improve awareness of fire risk to life and property.

2. Data

2.1. FMC field measurements

A total of 3,034 FMC field measurements taken in grasslands (955), shrublands (566), and forests (1,513) from 2001 to 2017 over 120 sites in Australia, China, Italy, Senegal, Spain, South Africa, Tunisia, and the USA validated the FMC retrieval methodology (Fig. 1). Table S1 in the *Supplementary Material* presents detailed information on these field sites while Table S2 and S3 illustrate the percentage of measurements in different seasons and fuel types for each country, respectively. The data is a subsample of Yebra et al. (2019)'s database and contains only sites with more than three consecutive FMC weekly measurements or only one time but at several nearby sites (e.g., Chinese sites), capturing the spatial instead of the temporal FMC variability.

2.2. Satellite data

2.2.1. MODIS products

Three MODIS products (Collection 6), MCD43A4, MCD15A3H, and MCD12Q1, were downloaded from the Land Processes Distributed Active Archive Center (LPDAAC) in the U.S. Geological Survey (USGS) Earth Resources Observation and Science Center (EROS) (http://lpdaac.usgs.gov). The MCD43A4 provides daily Bidirectional Reflectance Distribution Function (BRDF) corrected reflectance at 500 m spatial resolution rolling from 16-day composites. The "BRDF_Albedo_Band_Quality" quality flags layer of the MCD43A4 product kept only the 'good quality' full BRDF pixels with a zero value and removed all others with partial or complete cloud/shadow/snow cover or low quality data. To avoid possible errors in the geolocation of the MODIS product, the mean reflectance value of a 3 × 3-pixel window centered on the sampling sites was extracted for validation.

The MCD15A3H product provided the Leaf Area Index (LAI) to parameterize the RTMs. This product contains the entire time series from July 2002 to date and chooses the best available pixel from all the acquisitions of both MODIS sensors located on NASA's Terra and Aqua satellites within the 4 days. The "FparLai_QC" and "FparExtra_QC" layers selected the 'good quality' pixels without cloud, snow, and shadow for further analysis.

The International Geosphere-Biosphere Programme (IGBP) classification integrated in the MODIS land cover product MCD12Q1 Collection 6 (Sulla-Menashe et al., 2019) separated the grassland, shrublands (closed and open) and forests (evergreen needleleaf forest, evergreen broadleaf forest, deciduous needleleaf forest, deciduous broadleaf forest, mixed forest, woody savannas and savannas) fuel classes for global FMC mapping.

2.2.2. Landsat products

The surface reflectance Landsat 5 TM, 7 ETM+, and 8 OLI data integrated in Google Earth Engine (Gorelick et al., 2017) tested the homogeneity of each sampling site. Pixels marked as snow, cloud, and cloud shadow were not considered in the analysis. Each of these Landsat satellites has 16 days temporal resolution at a spatial resolution of at least 30 m. For the Jan 2001-Nov 2011 period, Landsat 5 TM was preferred over Landsat 7 ETM + unless Landsat 5 TM had poor quality due to cloud cover. Landsat 7 ETM + was used from Dec 2011 to Apr 2013, and afterward, the Landsat 8 OLI was used.

3. Methods

A methodological flowchart is shown in Fig. 2, including three steps. Firstly, RTMs were run forward for a specific range of the model parameters. These simulations built three LUTs from the model inputs parameters and reflectance outputs. Secondly, the backward inversion process tested different strategies to infer their influences on FMC retrieval. The optimal inversion strategy to produce FMC involved the

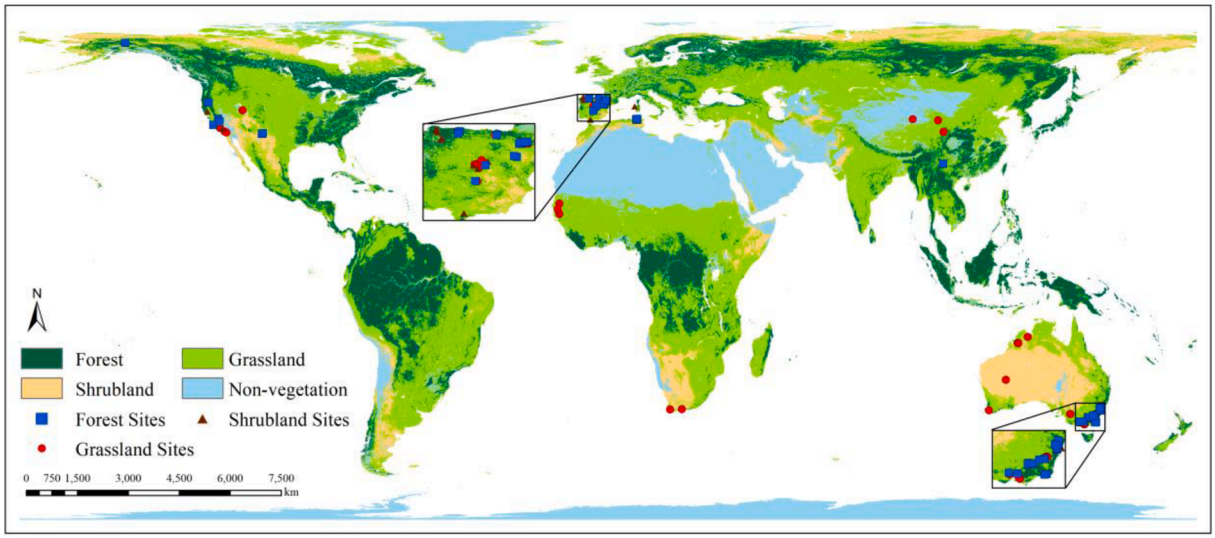

Fig. 1. Global grassland, shrubland, and forest distributions based on the International Geosphere-Biosphere Programme (IGBP) landcover type from the MODIS MCD12Q1 product with FMC sampling sites.

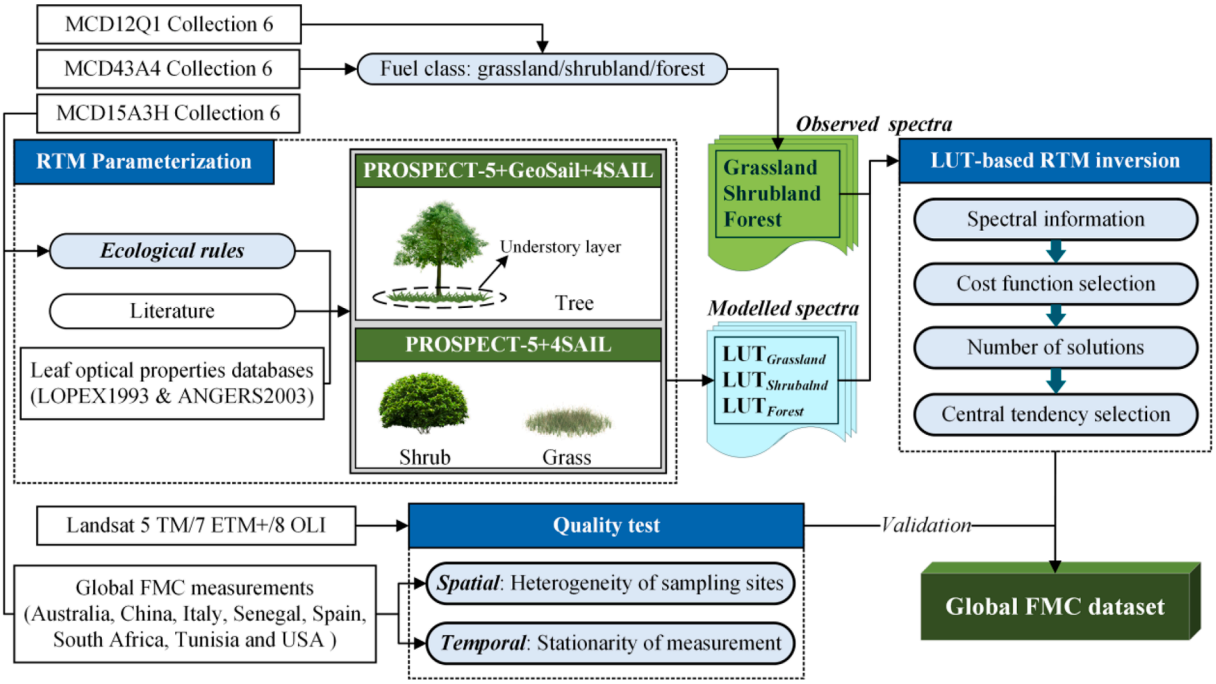

Fig. 2. Methodological flowchart to retrieve global FMC using RTMs and MODIS data.

investigation of (*i*) the selection of different spectral information to include in the computation of (*ii*) the selected cost functions, and (*iv*) the performance of different central tendencies in response to (*iii*) the selection of solutions. Thirdly, the exploration of temporal and spatial filtering rules removed low-quality field measurements from the validation database. Finally, the global FMC product was produced based on the optimal inversion strategy.

3.1. Global FMC model calibration

3.1.1. RTMs selection

PROSAIL RTM (http://teledetection.ipgp.jussieu.fr/prosail/) simulated grass and shrub canopies spectra following Yebra and Chuvieco (2009b) and Yebra et al. (2008). PROSAIL couples PROSPECT-5 leaf optics model (Feret et al., 2008) with 4SAIL (scattering by arbitrarily inclined leaves) canopy bidirectional reflectance model (Kuusk, 1991; Verhoef, 1984; Verhoef, 1998). The PROSPECT-5 simulates leaf-level reflectance and transmittance as a function of the following scattering and absorption components: leaf structure parameter (N, unit-less), C_{ab} (μg/cm^2), DMC (g/cm^2), EWT (g/cm^2), leaf brown pigment (C_{bp}, unit-less) and carotenoid content (C_{ar}, μg/cm^2). The 4SAIL model simulates the spectra of the canopy layer as a function of leaf inclination distribution function (LIDF), LAI (m^2/m^2), hot spot factor (hspot, unit-less), sun zenith angle (tts,), observer zenith angle (tto,), relative azimuth angle (psi,), leaf hemispheric reflectance (μ) and leaf transmittance (τ). The PROSAIL script used in this study integrates a spectral library of background soil surface with a parameter, psoil (unit-less), to characterize the effect of moisture and roughness condition in the soil

brightness (e.g., psoil = 0 represents a wet soil and psoil = 1 represents a dry soil). Additionally, the model script integrated six LIDFs: Planophile, Erectophile, Plagiophile, Extremophile, Spherical and Uniform. This script also offers an alternative way to characterize the LIDF using the average leaf angle (), where 0° and 90° indicate Planophile and Erectophile, respectively.

GeoSail model simulated forest reflectance, as it provides a realistic representation of heterogeneous and discontinuous vegetation with a low computational cost (Huemmrich, 2001). This model requires eight inputs: LIDF (unit-less), leaf-level spectral reflectance (μ) and transmittance (τ), LAI (m^2/m^2), the spectral reflectance of the background, solar zenith angle (tts, °), the shape of the crowns (either cylinder or cone), height to width ratio of the crown (CHW, unit-less) and crown coverage (ccov, unit-less). PROSPECT-5 simulated the leaf-level μ and τ.

GeoSail RTM assumes bare soil covers the forest understory. Instead, PROSAIL RTM simulated here this understory as a grass canopy. This process consists of changing the background soil reflectance in the shadow reflectance (ρ_s) and the illuminated background soil reflectance (ρ_b) in original Eq. (2) in Huemmrich (2001),

$$\rho_t = C\rho_c + S\rho_s + B\rho_b \quad (2)$$

where ρ_t is the total scene reflectance for forest canopy,ρ_c *is* the canopy reflectance, S is the fraction of the shadowed background, B is the fraction of the area that is illuminated background and C is the fraction covered by the solids, i.e., the canopy coverage. Here, the ρ_s and ρ_b were replaced by the canopy reflectance of understory grass that was modeled by the PROSAIL RTM. The diffuse radiation was set as the dominant radiation for the understory grass with the hypothesis that the tree canopy intercepted most of the direct radiation. In this case, the PROSAIL bi-hemispherical reflectance, rather than the BRDF, simulated the understory grass and replaced the Lambertian soil background originally integrated in GeoSail. The variation of understory reflectance in response to the change of the solar zenith angle, observer zenith angle, and relative azimuth angle can be ignored (Fig. S1 in *Supplementary Material*).

3.1.2. RTMs parameterization

RTMs were parameterized using different ranges of values for grassland, shrubland, and forest based on prior knowledge from the literature, laboratory experiments, field campaigns, sensitivity analysis of the input parameters of PROSAIL (Bowyer and Danson, 2004) and GeoSail and open-source satellite products (Table 1). The ranges for tts, tto, and psi for grassland, shrubland, and tree canopy followed Yebra et al. (2008). Fixed values for those angles parameterized the forest understory layer since the results of the sensitivity analysis demonstrated that their effects on canopy reflectance are slight (Fig. S1 in *Supplementary Material*). LAI ranged from 0 to 7 for grass (mean: 1.12, standard deviation: 1.21) and shrub (mean: 1.76, standard deviation: 1.56) and from 0 to 5 for forest (mean: 1.67, standard deviation: 1.23) based on the values extracted from the MCD15A3H MODIS LAI product (Myneni et al., 2002) over the field sites and sampling dates. Following Houborg et al. (2009), the hspot was set as a function of LAI. The psoil ranged from 0 (wet soil) to 1 (dry soil). The LIDF was erectophile, spherical and planophile for grassland (Wang et al., 2013; Yebra et al., 2008), plagiophile, erectophile and spherical for forest (Jurdao et al. 2013) and from 50° to 90° for shrubland (Casas et al. 2014). CHW ranged from 1 to 3, ccov from 0.2 to 1 and crown forest shapes were cone and cylindrical (Jurdao et al., 2013; Quan et al., 2017a).

The parameterization of the N, C_{ab}, EWT, DMC, C_{bp} and C_{ar} to simulate leaf reflectance and transmittance of grass, shrub, tree and understory layer in PROSPECT-5 model followed previous studies (Casas et al., 2014; Quan et al., 2015; Quan et al., 2017a; Yebra et al., 2008) and measurements from LOPEX1993 (Hosgood et al., 1995) and ANGERS2003 (Feret et al., 2008) leaf optical properties databases.

To simulate the canopy spectra of the understory layer with PROSAIL, a prior study from Quan et al. (2017a) applied LAI values of 0, 1 and 2 (where LAI = 0 indicates the forest background is bare soil); and EWT values of 0.005, 0.01 and 0.02. The other parameters were set as fixed values given that (*i*) they are normally insensitive to the RTM outputs (Fig. S2) and (*ii*) the RTM inversion becomes unstable and ill-posed with too many free parameters (Combal et al., 2003a; Verhoef and Bach, 2007).

Besides, the maximum and minimum values observed in the field (Table S1) also constrained the FMC ranges for grassland (1% to 450%), shrubland (1% to 250%), and forest (1% to 250%). Subsequently, the model assumed a Gaussian distribution for the LAI, N, C_{ab}, EWT and DMC, whereas a uniform distribution for the other parameters (tts, psoil and LIDF for shrubland case) was preferred due to the lack of enough information to characterize their probability distribution.

3.1.3. Realistic FMC simulation scenario using ecological rules

The RTMs input variables are not independent of each other but naturally correlated (Yebra and Chuvieco, 2009b). If RTMs assume their input parameters are fully independent, spurious combinations may produce unrealistic spectra. This issue confuses the inversion process and aggravates the ill-posed inversion problem. To alleviate such a problem, ecological rules regularized the RTMs to make the FMC simulation scenario more realistic. The ecological rules refer to the natural linear or non-linear relationships between vegetation biophysical and biochemical variables. For instance, low FMC very rarely coincides with high C_{ab} or low DMC, since plants with water stress tend to reduce the photosynthetic activity and increase DMC (Yebra and Chuvieco, 2009b).

The global FMC field measurements (Table S1) provided the information to build the ecological rules together with LAI values extracted from the MCD15A3H product (LAI vs. FMC), as well as EWT, DMC and C_{ab} values from the LOPEX1993 and ANGERS2003 databases. These databases all together include a large set of vegetation species. Fig. 3 and 4 demonstrate strong LAI vs. FMC ($r = 0.71$, $p < 0.01$) and C_{ab} vs. DMC ($r = 0.58$, $p < 0.01$) relationships for grassland and EWT vs. DMC ($r = 0.66$, $p < 0.01$) and C_{ab} vs. DMC ($r = 0.52$, $p < 0.01$) for forest but weak LAI vs. FMC ($r = 0.35$, $p < 0.01$) for forest and C_{ab} vs. EWT ($r = 0.23$, $p < 0.01$) for shrubland. The rest variable combinations rendered no significant relation ($p > 0.01$) and, therefore, they were not considered. The RTMs modeling phase introduced these relationships by sampling and simulating more likely variable combinations with higher correlations than the lower ones. For this, it calculated the joint posterior probability distribution of the variable combinations using Eq. (3):

$$f(x,y) = \left(1 - \frac{g(x,y)}{MAX(|g(x,y)|)}\right)^{r\times k} \quad (3)$$

where the $f(x,y)$ is the joint posterior probability distribution of x and y; $g(x,y)$ is the fitted function in Figs. 3 and 4; r is the correlation coefficient and k is a controlling factor that a higher k value can generate more constrained variable combinations (Fig. S3 and $k = 10$ in this study). This approach removed unrealistic simulation scenarios. For example, higher LAI is unlikely to correspond to a lower FMC for grasslands (Fig. 3). Finally, a LUT for each fuel class was generated by running the RTMs forward using MATLAB software R2017a version (The Mathworks; Natick, MA, USA; www.mathworks.com).

3.2. LUT-based RTM inversion

The inversion searches within the LUT to find the most similar simulated spectra to the observed spectra. This process requires making decisions involving (*i*) the spectral information included, (*ii*) the selection of the cost function, (*iii*) the percentage of solutions from the cost function, and (*iv*) the measurement of central tendency to ensemble them. Different options for i to iv were explored to find the optimal inversion strategy.

Table 1
Input parameters for the parameterization of the RTMs to simulate spectra for the three fuel classes.

RTMs	Parameters	Units	Symbol	Grassland Parameterization	Sources	Shrubland Parameterization	Sources	Forest Parameterization		Sources
GeoSail(Tree canopy level)	Sun zenith angle	(°)	tts					27 – 51		Yebra et al. (2008)
	Leaf area index	m^2/m^2	LAI					0 – 5(1.67, 1.23)		MCD15A3H product
	Leaf inclination distribution function (LIDF) type		LIDF					PlagiophileErectophileSpherical		Jurdao et al. (2013)
	Height to width ratio of the crown		CHW					1 – 3		Quan et al. (2017)
	Crown coverage		ccov					0.2 – 1.0		Quan et al. (2017)
	Shape of the crowns							Cone/cylindrical		Jurdao et al. (2013)
4SAIL(Grass and shrub canopy level)	Sun zenith angle	(°)	tts	27 – 51	Yebra et al. (2008)	27–51	Yebra et al. (2008)	/		This study
	View zenith angle	(°)	tto	5	Yebra et al. (2008)	5	Yebra et al. (2008)	/		This study
	Relative azimuth angle	(°)	psi	−30	Yebra et al. (2008)	−30	Yebra et al. (2008)	/		This study
	Leaf area index	m^2/m^2	LAI	0 – 7(1.12, 1.21)	MCD15A3H product	0 – 7(1.76, 1.56)	MCD15A3H product	0, 1 and 2		Quan et al. (2017)
	Hot spot factor	/	hspot	0.5/LAI	Quan et al. (2015)	0.01	Casas et al. (2014)	0.5/LAI		Quan et al. (2017)
	Soil factor	/	psoil	0 – 1	Quan et al. (2015)	0 – 1	Quan et al. (2015)	0.5		Quan et al. (2017)
	Leaf inclination distribution function or average leaf angle	/	LIDF	Erectophile, Spherical, Planophile	Wang et al. (2013)	50 – 90	Casas et al. (2014)	Spherical		Quan et al. (2017)
PROSPECT-5 (Leaf level)								Overstory	Understory	
	Leaf structure parameter	/	N	1.1 – 3(**1.7**, 0.32)	Angers2003&LOPEX1993	1.27–3(1.79, 0.36)	Angers2003&LOPEX1993	1.05 – 2.74 (1.54, 0.27)	**1.7**	Angers2003&LOPEX1993
	Chlorophyll *a* + *b* content	$\mu g/cm^2$	C_{ab}	1.36 – 98.80 (**43.50**, 19.29)	Angers2003&LOPEX1993	0.78 – 77.53 (35.37, 22.02)	Angers2003&LOPEX1993	0.87 – 106.72 (41.13, 20.63)	**43.5**	Angers2003&LOPEX1993
	Leaf equivalent water thickness	g/cm^2	EWT	0.0001 – 0.036 (0.0131, 0.0071)	Angers2003&LOPEX1993 &Yebra et al. (2008)	0.0001 – 0.052 (0.011, 0.061)	Angers2003&LOPEX1993 &Casas et al. (2014)	0.001 – 0.029 (0.0098, 0.0037)	0.005, 0.01, 0. 02	Angers2003&LOPEX1993 & Quan et al. (2017)
	Dry matter content	g/cm^2	DMC	0.0017 – 0.0096 (**0.0042**, 0.0018)	Angers2003&LOPEX1993	0.0017 – 0.033 (0.0053, 0.0033)	Angers2003&LOPEX1993	0.0018 – 0.0189 (0.0052, 0.0027)	**0.0042**	Angers2003&LOPEX1993
	Brown pigment	/	C_{bp}	0	Quan et al. (2015)	0	Quan et al. (2015)	0	0	Quan et al. (2015)
	Carotenoid content	$\mu g/cm^2$	C_{ar}	8	Casas et al. (2014)	10	Casas et al. (2014)	10	8	Casas et al. (2014)

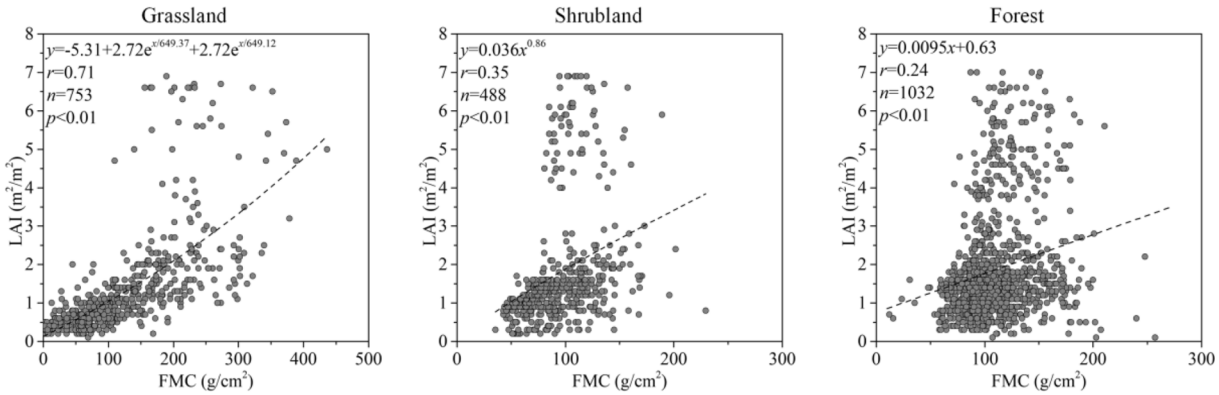

Fig. 3. Relations between FMC field samples and LAI values extracted from the corresponding MCD15A3H product for three fuel classes.

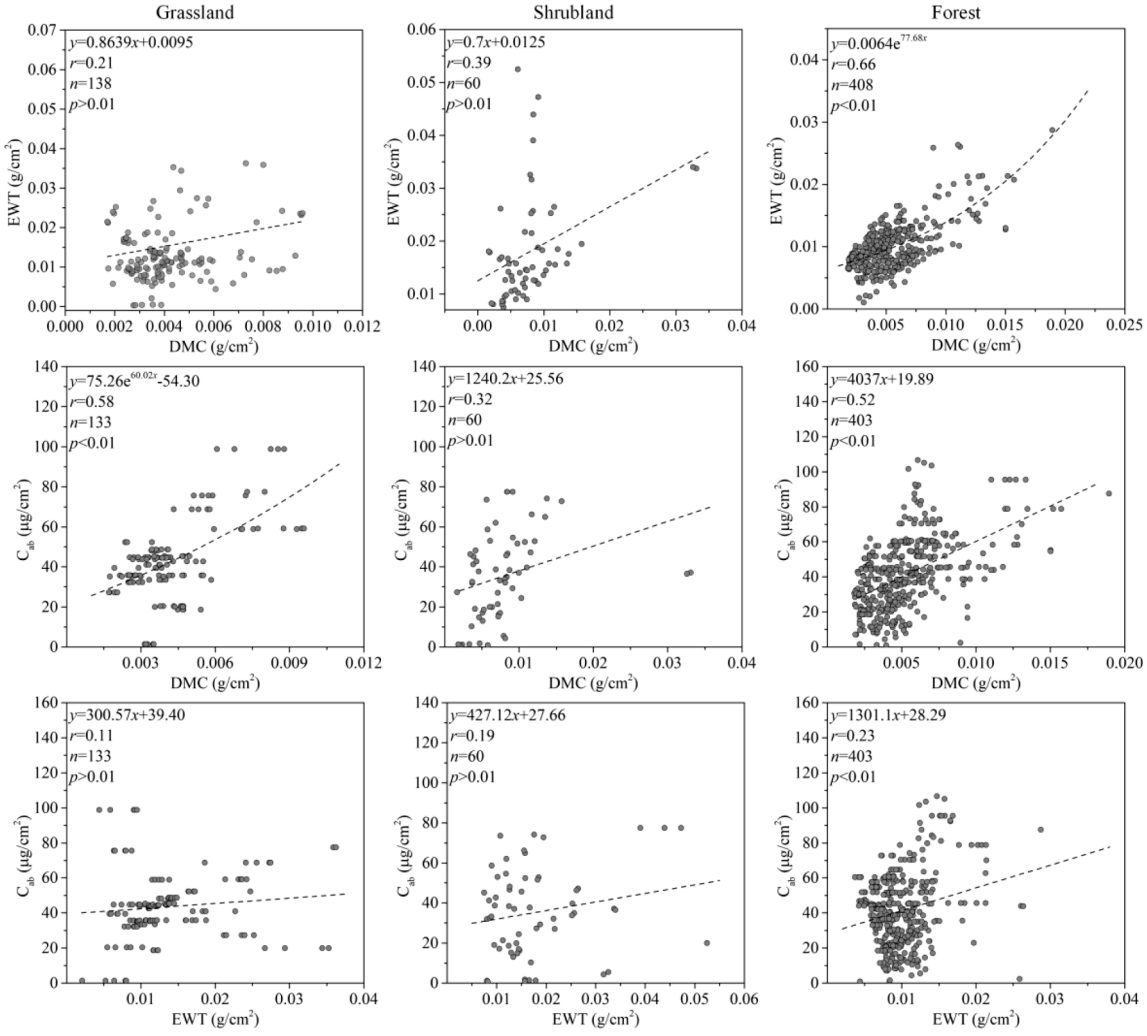

Fig. 4. Relations among EWT, DMC, and C_{ab} for the three fuel classes (values obtained from the LOPEX1993 and ANGERS2003 databases).

3.2.1. *Spectral information*

The FMC retrieval tested seven MCD43A4 spectral bands and 12 VIs, hereafter simplified as the spectral information (Table 2). R^2 and RMSE values between observations and retrievals assessed the performance of this spectral information. This test firstly checked each variable independently and then all their combinations. Secondly, a jackknife approach removed the spectral information one at a time from all combinations to determine the optimal spectral information. The model kept this variable only if R^2 decreased and RMSE increased, as it had a positive effect on the FMC retrieval. Finding the final optimal combinations relied on repeating this step until removing spectral information showed no further improvement in FMC retrieval.

3.2.2. *Cost function*

The direct LUT spectra comparison against observed spectra through a cost function constitutes the most common model inversion approach

Table 2
VIs for FMC retrieval and calculated based on the MCD43A4 Collection 6 reflectance band 1 ~ 7.

VIs	Equations	References
Normalized Difference Infrared Index	NDII=(Band2 – Band6)/ (Band2 + Band6)	Hardisky et al. (1983)
Normalized Difference Infrared Index7	$NDII_7$=(Band2 – Band7)/ (Band2 + Band7)	
Normalized Difference Vegetation Index	NDVI=(Band2 – Band1)/ (Band2 + Band1)	Tucker (1979)
Enhanced Vegetation Index	EVI = 2.5(Band2 – Band1)/ (Band2 + 6Band1-7.5Band3 + 1)	Huete et al. (2002)
Normalized Difference Tillage Index	NDTI=(Band6 – Band7)/ (Band6 + Band7)	van Deventer et al. (1997)
Visible Atmospheric Resistant Index	VARI=(Band4 – Band1)/ (Band4 + Band1 – Band3)	Gitelson et al. (2002)
Normalized Difference Water Index	NDWI=(Band2 – Band5)/ (Band2 + Band5)	Gao (1996)
Global Environmental Monitoring Index	GEMI = [μ(1 – 0.25μ) – (Band2 – 0.125)]/ (1 – Band4),μ = [2($Band1^2$ – $Band2^2$) + 1.5Band1 + 0.5Band2]/ (Band1 + Band2 + 0.5)	Pinty and Verstraete (1992)
Global Vegetation Moisture Index	GVMI = [(Band2 + 0.1) – (Band6 + 0.02)]/ [(Band2 + 0.1) + (Band6 + 0.02)]	Ceccato et al. (2002)
Moisture Stress Index	MSI = Band6/ Band2	Rock et al. (1986)
Greenness index	G_{ratio} = Band4/ Band1	Zarco-Tejada et al. (2005)
Three-band spectral indices	3BSI=(Band4 – Band7)/ (Band5 + Band7)	Verrelst et al. (2015)

(Verrelst et al., 2014; Verrelst et al., 2015). Leonenko et al. (2013) suggested that different cost functions may provide different robustness to estimate biophysical parameters. The availability of many cost functions gives a high degree of flexibility since it allows model optimization for a wide range of error distributions. Given this, the above-described studies showed how cost functions impact the model performance to retrieve LAI, leaf chlorophyll content, fractional vegetation cover and the fraction of photosynthetically active radiation absorbed by the green parts of the vegetation canopy. Meanwhile, no studies to date explicitly evaluate the effect of these cost functions on FMC estimates. Therefore, this study assessed 12 cost functions in the retrieval of FMC to find the best estimate by solving the minimization problem (Table 3).

3.2.3. Percentage of solutions

The similarity between the simulated spectra from the LUT and the observed spectral information ranked the $f(v,w)$ solutions generated from the cost function. The retrieved FMC value came from the central tendency (see section 3.2.4) of a large 'ensemble' of FMC values in the LUT corresponding to an ensemble of 'near-optimal' ranked $f(v,w)$ solutions. This study tested how the 'ensemble' selection affected the FMC retrievals. Rather than adopting the number as the 'ensemble' as normally presented in previous literature (Yebra et al., 2018a), the percentage of the ranked $f(v,w)$ solutions from 1 to 100% were investigated and compared, where 1 indicated the minimum $f(v,w)$ one solution and 100% meant using all the solutions.

3.2.4. Central tendency

The retrieved FMC depended on the central tendency values of the percentage of the ranked $f(v,w)$ solutions. This study tested six central tendencies, including the arithmetic mean ($\overline{FMC}_A$, Eq.4), the median value (FMC_m), the geometric mean ($\overline{FMC}_G$, Eq.5), the harmonic mean ($\overline{FMC}_H$,Eq.6), the quadratic mean ($\overline{FMC}_Q$,Eq.7), and the mode (FMC_o, Eq. (8)).

$$\overline{FMC}_A = \frac{\sum_{i=1}^{n} FMC_i}{n} \tag{4}$$

$$\overline{FMC}_G = \left[\prod_{i=1}^{n} FMC_i\right]^{1/n} \tag{5}$$

$$\overline{FMC}_H = \frac{n}{\sum_{i=1}^{n} \frac{1}{FMC_i}} \tag{6}$$

$$\overline{FMC}_Q = sqrt\left[\frac{\sum_{i=1}^{n} FMC_i^2}{n}\right] \tag{7}$$

$$FMC_o = \overline{FMC}_A - 3(\overline{FMC}_A - FMC_m) \tag{8}$$

where i is the i^{th} value (default: $i = 1$) in the derived FMC solution, and n is the total number of the ranked $f(v,w)$ solutions.

Table 3
Cost functions assessed. v denotes the bands or VIs from satellite data and w denotes the modeled bands or VIs. * Cost functions modified from their original form, using absolute values to avoid the negative ones that may cause the calculation to collapse.

Cost functions	Equations	References
Root-mean-square error ($RMSE_f$)	$f(v,w) = \sqrt{\frac{\sum_{i=1}^{n}(v_i - w_i)^2}{n}}$	Darvishzadeh et al. (2008)
Spectra angle (SA)	$f(v,w) = cos^{-1}\left(\frac{\sum_{i=1}^{n} v_i w_i}{\sqrt{\sum_{i=1}^{n} v_i^2}\sqrt{\sum_{i=1}^{n} w_i^2}}\right)$	Kruse et al. (1993)
Least absolute error (LAE)	$f(v,w) = \sum_{i=1}^{n} \lvert v_i - w_i \rvert$	Verrelst et al. (2015)
*Shannon (1948) (S1948)	$f(v,w) = \lvert - \sum_{i=1}^{n}(\frac{v_i + w_i}{2})\ln(\frac{v_i + w_i}{2}) + \frac{1}{2}\sum_{i=1}^{n}(v_i\ln(v_i) + w_i\ln(w_i))\rvert$	Verrelst et al. (2015)
L-divergence lin (LDL)	$f(v,w) = \sum_{i=1}^{n}(v_i\ln(v_i + w_i)\ln(2w_i - v_i)\ln(\frac{v_i + w_i}{2}))$	Verrelst et al. (2015)
Bhattacharyya divergence (BD)	$f(v,w) = -\ln(1 + \sum_{i=1}^{n}(\sqrt{v_i w_i} - \frac{v_i + w_i}{2}))$	Verrelst et al. (2015)
*Jeffreys–Kullback–Leible (JKL)	$f(v,w) = \sum_{i=1}^{n} \lvert (v_i - w_i)\rvert\lvert \ln(v_i) - \ln(w_i)\rvert$	Verrelst et al. (2015)
*Neyman chi-square (NCS)	$f(v,w) = \sum_{i=1}^{n} \frac{(v_i - w_i)^2}{\lvert v_i \rvert}$	Verrelst et al. (2015)
*Pearson chi-square (PCS)	$f(v,w) = \sum_{i=1}^{n} \frac{(v_i - w_i)^2}{\lvert w_i \rvert}$	Verrelst et al. (2015)
Normal distribution-LSE (NDL)	$f(v,w) = \sum_{i=1}^{n}(v_i - w_i)^2$	Verrelst et al. (2015)
Geman and McClure (GM)	$f(v,w) = \sum_{i=1}^{n} \frac{(v_i - w_i)^2}{(1 + (v_i - w_i)^2)}$	Verrelst et al. (2015)
*Exponential (Exp)	$f(v,w) = \sum_{i=1}^{n} \lvert w_i(\exp(-\frac{v_i - w_i}{w_i}) - 1)\rvert$	Verrelst et al. (2015)

3.3. Validation

The stability of FMC measurements in consecutive observations and homogeneity for each site tested the data quality to be used for validation. For the former one, a temporal rule (Eq. (9)) filtered out the abnormal values in the scale of 3 consecutive FMC observations following Yebra et al. (2018a).

$$\frac{FMC_i - \mu}{\sigma} < x \tag{9}$$

where FMC_i is the i^{th} FMC value in 3 consecutive FMC observations, μ is their median value, σ is the standard deviation across the time series, and x is the critical value. Lymburner et al. (2011) applied Eq. (9) to filter out spikes in VIs time series for landcover classification and suggested $x = 2.1$. Subsequently, Yebra et al. (2018a) applied a more restrictive value $x = 1$ to better avoid unrealistic abrupt changes in FMC within consecutive sampling dates. In this study, x ranged from 0.4 (most strict) to 3 (no filter). Notably, Eq. (9) requires at least three FMC measurements in a site. For each coordinate in China, the FMC was only sampled once and therefore Eq. (9) was not applied.

The coefficient of variation (CV, %) provided in the global field measured FMC database by Yebra et al. (2019) assessed the site homogeneity. CV was calculated as the ratio of the standard deviation and mean NDVI of all the Landsat pixels within a 500 × 500 m buffer that matched the MODIS pixel size ($CV_{Landsat}$, Eq. (10)) using Google Earth Engine (Gorelick et al., 2017) as,

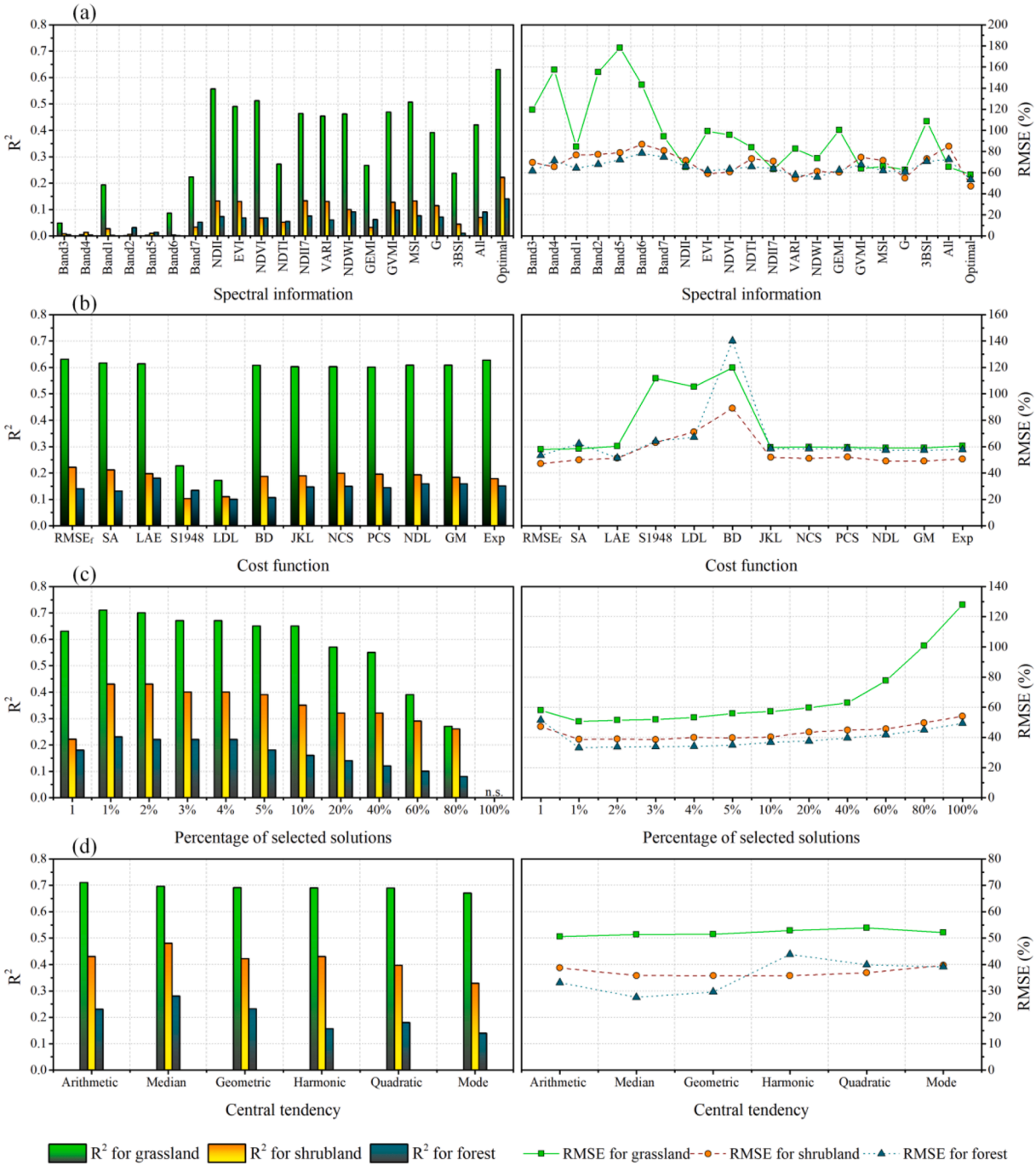

Fig. 5. R^2 and RMSE between FMC field measurements and retrievals for different fuel classes and using (a) different spectral information, (b) cost functions, (c) percentage of selected solutions, and (d) central tendency.

$$\frac{NDVI_{Std,500mbuffer}}{NDVI_{mean,500mbuffer}} \times 100\% < CV_{Landsat} \quad (10)$$

where $NDVI_{Std,500mbuffer}$ and $NDVI_{mean,500mbuffer}$ denote the NDVI standard deviation and mean value of all the Landsat pixels (Landsat 5 TM, 7 ETM+, or 8 OLI) within the buffer corresponding to MODIS pixel size, respectively. *CV* ranged from 5 (most strict) to 50 (no filter).

4. Results

4.1. Evaluation of FMC estimates from different RTM inversion strategies

Starting with an evaluation of the spectral information for the inversion (Fig. 5 a), all the VIs outperformed the original MODIS bands for the FMC retrieval for all three fuel classes. Among them, the NDII, EVI, NDVI, $NDII_7$, VARI, NDWI, GVMI and MSI performed well for grassland; NDII, EVI, $NDII_7$, VARI, GVMI, MSI and G_{ratio} for shrubland, and NDII, EVI, $NDII_7$, NDWI, GVMI and G_{ratio} for forest sites. When using all bands and VIs at the same time for the FMC retrievals, the accuracy levels did not significantly improve compared to the performance of single VIs (e.g., NDII worked the best for grassland and shrubland, and NDWI for forest). However, simultaneously selecting the best performing VIs improved the retrieval results in comparison to using a single VI. More interestingly, when simultaneously combining G_{ratio} with other VIs, FMC estimates improved for all three fuel classes (Fig. 5 a). The final optimal VIs combinations were then the EVI, NDVI, NDII, MSI and G_{ratio} for grassland; NDII, EVI, VARI and G_{ratio} for shrubland; and NDII, EVI, GVMI and G_{ratio} for the forest.

The evaluation of different cost functions revealed that all of them generally performed similarly except S1948, LDL and BD that resulted in the highest RMSE values for all the fuel classes (Fig. 5 b). More in detail, the $RMSE_f$ and Exp cost functions outperformed the others for grassland. However, $RMSE_f$ has a higher computational efficiency than Exp due to its simpler equation (Table 3). The $RMSE_f$ also worked well for shrubland, whereas LAE outperformed the others for forest (Fig. 5 b). Therefore, the final optimal cost functions were $RMSE_f$ for grassland and shrubland, and LAE for the forest.

With the increase from the first minimum of one to 100% $f(v,w)$ solutions, the FMC retrieval accuracy increased with R^2 to its maximum at 1%, slowly decreased up to 10%, with a sharp decrease from 10% to 20% and a significant drop from 40% on to 100% solutions. Conversely, the RMSE reached its minimum at 1%, slightly increased up to 40%, and increased drastically from 40% on to 100%. All three fuel classes have a similar trend, but grasslands have the widest variation (Fig. 5 c). Among all options tested, the 1% of $f(v,w)$ solutions kept the highest R^2 and the lowest RMSE and therefore was selected for the product.

Among the six measures of central tendencies explored (Fig. 5 d) the median worked better for FMC retrieval than the other central tendencies for grassland ($R^2 = 0.70$, RMSE = 51.06%, $p < 0.01$) and forest ($R^2 = 0.28$, RMSE = 27.60%, $p < 0.01$) and was selected for the generation of the FMC product. However, the median was selected for shrubland given a slightly higher R^2 than the harmonic mean ($R^2 = 0.48$, RMSE = 35.83%, $p < 0.01$).

Table 4
Detailed information on the number of field measurements (n), R^2 and RMSE between observed and estimated FMC values for grassland, shrubland and forest with the selection of *none*, *optimal* and *strict* *x* and CV_{Lansat} filter rules ($p < 0.01$).

Filter rule	Fuel class	*x*	$CV_{Landsat}$	n	R^2	RMSE (%)
None	Grassland	/	/	955	0.71	50.86
	Shrubland	/	/	566	0.48	26.83
	Forest	/	/	1315	0.27	27.60
	All			3034	0.62	34.57
Optimal	Grassland	2.2	15	765	0.75	44.00
	Shrubland	1.7	30	408	0.59	22.09
	Forest	1.5	20	835	0.45	21.53
	All			2008	0.71	32.36
Strict	Grassland	0.5	10	449	0.74	45.92
	Shrubland	0.5	10	195	0.51	23.78
	Forest	0.5	10	414	0.33	21.25
	All			1058	0.69	34.05

4.2. Global FMC validation

Different combinations of *x* (Eq. (9)) and $CV_{Landsat}$ (Eq. (10)) filtered out anomalous FMC values measured in the field. When *no filter rule* was applied, the results were the worst, followed by the *strict rule* and then the optimal filter that obtained the highest R^2 and lowest RMSE values for the three fuel classes (Table 4). When pooling all fuel classes together, the total number of measurements available for validation decreased from 3,034 to 2,008 and 1,058 cases for *none*, *optimal* and *strict* filtering, respectively. The *optimal filter rule* also rendered the best accuracy ($R^2 = 0.71$, RMSE = 32.36%, $p < 0.01$) (Table 4 and Fig. 6).

4.3. Global FMC mapping

The daily global FMC maps from 2001 to 2019 were produced based on the best inversion strategy for each fuel class using the high-performance parallel computing platform of the University of Electronic Science and Technology of China. This dataset can be accessed via https://firewatching.cn/world_FMC. Given storage limitations, the FMC product was stored in 8 days interval instead of daily. Fig. 7 shows the global three-month median composite FMC maps at 500 m from 2017 to 2018 as an example while Fig. 8 illustrates the average FMC curves for different latitudes, fuel classes and periods in terms of the maps in Fig. 7. Overall, the grassland FMC curves rendered the highest dynamics during the four periods, followed by the shrubland and forest curves.

Over 33°N latitude and between 8°N and 5°S, the highest grassland FMC was observed in the Jun-July-Aug period and the lowest in Dec-Jan-Feb (Fig. 8). The grassland FMC increased from 33°N to 18°N latitude, except for the Mar-Apr-May period when the FMC decreased. Noted that here the highest grassland FMC occurred in the Sep-Oct-Nov rather than the Jun-Jul-Aug as commonly recognized. Between the 18°N and 8°N, a sharp drop in grassland FMC was observed. This phenomenon also appeared in the shrubland case between 22°N and 8°N. For the region between 5°S and 32°S, Mar-Apr-May was the highest FMC period, whereas Sep-Oct-Nov was the lowest grassland FMC (Fig. 7). Below 32°S latitude, the Sep-Oct-Nov and Dec-Jan-Feb were the highest and lowest FMC periods, respectively. For both the shrubland and forest over 55°N latitude, the highest and lowest FMC periods were the Mar-Apr-May and Dec-Jan-Feb, respectively. Between 20°S and 40°S latitude, the shrubland FMC curves in the four periods did not change much. Below 56°N latitude, forest FMC did not show significant dynamics during the four periods observed.

5. Discussion

5.1. Model development and the inversion strategy selection

PROSAIL RTM modeled FMC on grassland and shrubland and provided a good performance (Fig. 6). This model was built for a turbid-medium plane-parallel simulation and specifically designed to best fit a continuous cover structure (Verhoef, 1984), such as grassland. Thus, it is theoretically not suitable for the discontinuous and heterogeneous shrubland, particularly for an open shrubland type. Nevertheless, previous literature also reported the feasibility of this RTM to retrieve shrubland FMC (Casas et al., 2014; Trombetti et al., 2008; Yebra et al., 2018a).

The PROSPECT-5 RTM was designed for simulating the reflectance and transmittance of a broadleaf while the LIBERTY RTM was for needle leaf (Dawson et al., 1998). This study only applied the PROSPECT-5 RTM for all the needle and broad leaves, since previous studies showed that the PROSPECT-5 RTM was still reasonable for retrieving

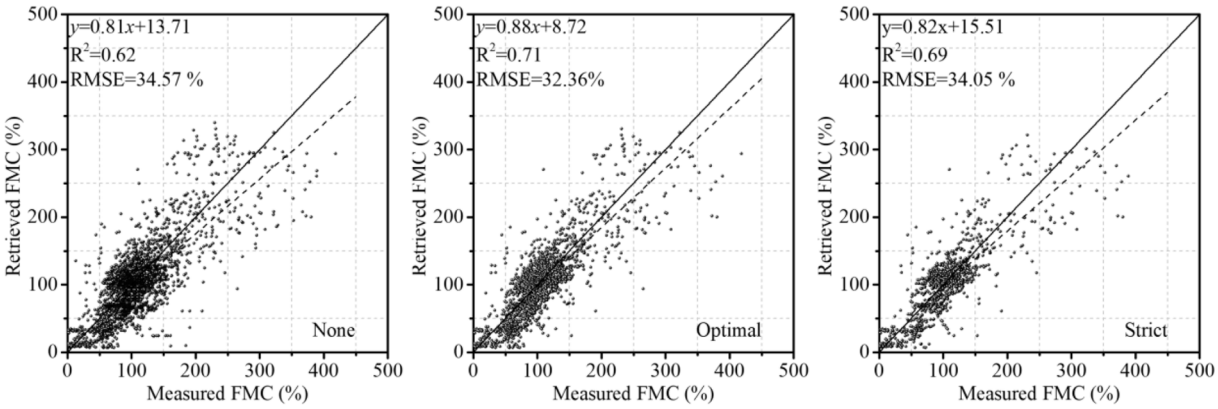

Fig. 6. FMC estimates vs. measurements when selecting *none* (left), *optimal* (center) and *strict* (right) × and CV_{Lansat} filter rules ($p < 0.01$).

canopy water content, chlorophyll content and burn severity for needle leaf (Cheng et al., 2006; De Santis et al., 2009; Zarco-Tejada et al., 2004).

The multiple ecological information was considered which led to more realistic RTMs simulated scenarios. Linear relationships integrated this information on previous studies (Jurdao et al., 2013; Quan et al., 2017b; Yebra and Chuvieco, 2009b) or also using a correlation matrix (Feret et al., 2011; Quan et al., 2015). The linear relationship can only characterize the relations for two inputs. Meanwhile, a correlation matrix can simultaneously characterize the relations between multiple RTM inputs, but the relationship between each input in the matrix is essentially linear. While relations between RTM inputs were normally none-linear, such as the LAI vs. FMC and EWT vs. DMC (Fig. 3 and 4). This study utilized a new method, i.e., Eq. (3), to characterize the non-linear relationship between RTM inputs. The correlation test validated the statistical relationship between these variables were significant ($p < 0.01$) or not ($p > 0.01$). Afterward, Eq. (3) was used to integrate the correlation into the RTM modeling phase by sampling the variable combinations. A higher *r*-value illustrated in Fig. 3 and 4, a strict sampling strategy was made (Fig. S3). This method can avoid introducing big bias into the FMC retrieval even for a low *r*-value, unless no significant correlation was found ($p > 0.01$). That is, the combinations of RTM inputs with high posterior probability are more likely sampled and vice versa. Thus, this method can more realistically model the relationships between each one of the model inputs.

The relations between model-free parameters are different between this work and previous studies. For example, Fig. 4 showed that there was no significant correlation ($p > 0.01$) between EWT and DMC for grass and shrub species based on the LOPEX1993 and ANGERS2003 datasets. However, our previous studies found that there was a positive correlation between EWT and DMC ($R^2 = 0.46$, $p < 0.01$) for the alpine wetlands located in western China in the Summer season (Quan et al., 2017b), with a similar degree as reported by Feret et al. (2011). Therefore, a universal and representative way of characterizing the ecological information is preferred for reliable global-scale FMC mapping. This is the reason to use LOPEX1993 and ANGERS2003 datasets, as they comprise diverse leaf properties from a large number of vegetation species.

In the backward inversion process, the LUT algorithm was used to derive the FMC from the MCD43A4 product. A key aspect of this study was the selection of the best performing inversion strategy for different fuel classes. For the selection of spectral information, a single VI presented superior accuracy than a single band, whereas when all the bands and VIs were used together, the accuracy level did not improve significantly. Furthermore, this study confirmed previous researches that NDII can be a good indicator for FMC retrieval of these three fuel classes (Fig. 5) due to the strong absorption features of water in the near- and shortwave-infrared spectral regions (Caccamo et al., 2012; García-Haro et al., 2020; Jurdao et al., 2013; Yebra and Chuvieco, 2009b; Yebra et al., 2008; Yebra et al., 2018a). The EVI and G_{ratio} were also found to perform well to retrieve FMC for these three fuel classes even they do not include the short-wave band. The likely cause is spatial and temporal variation in response to the FMC dynamics in the vegetation canopy structure and pigment, e.g., LAI and C_{ab} (Bowyer and Danson, 2004). Compared to the spectral band, VIs can minimize the topographic effects and influence from background soil on the reflected radiance (Liao et al., 2015; Matsushita et al., 2007). Additionally, the three-band spectral index (3BSI) suggested by Verrelst et al. (2015) worked well for LAI retrieval but was not suitable here for FMC retrieval.

5.2. Validation of the global product

The accuracy of the FMC retrievals highly improved when filtering out the FMC observations from heterogeneous sites within the MODIS footprint and abnormal values in 3 consecutive FMC observations (Table 4 and Fig. 6), revealing that the methods proposed to assess the stationarity and heterogeneity of the field sites were effective. Usually, studies consider FMC measurements taken at the field as the "ground truth" values for the validation purpose, yet uncertainties inevitably existed. Yebra et al. (2018a) reported the factors causing these uncertainties, such as the FMC sampling after rain or dew events; the inclusion of fruits, galls or twigs other than leaves; or the different proportion of juveniles and adults leaves sampled. Matthews (2010) also pointed out that the drying temperature also has a significant effect on the oven-dry mass (i.e., affect FMC) of dead grass, pine and eucalyptus fuels. Cheng et al. (2014) furtherly showed that the diurnal declines of canopy water content also introduce uncertainties on FMC retrievals.

Moreover, applying the restrictive filter decreased the number of measurements for all fuel classes (Table 4), particularly for forests (1315 to 414 cases), followed by shrubland (566 to 195) and grassland (955 to 449). This proves that the FMC measurements in forest sites are highly heterogeneous. Taking representative samples in the forest is far more complex and time-consuming than in grassland and shrubland. The top of the canopy should be more closely related to optical remote sensing, but it requires the use of a slingshot or similar devices to reach these leaves at the top (Youngentob et al., 2016). Besides, the forest deep root system reduces the seasonal FMC variation in comparison to grassland and shrubland (see Table S1), making it more difficult to validate. Moreover, forest can also have an understory grass and shrub layer (García-Haro et al., 2020). Hence, the reflectance from grass and shrub mixed with overstory forest canopy results in more impure mixed pixels. The coupled RTM was set to model this, but the higher dimensional unknown inputs of this coupled RTM, compared to the grassland and shrubland (Table 1), may aggravate the forest FMC retrieval uncertainty.

Additionally, FMC field measurements used for the validation were

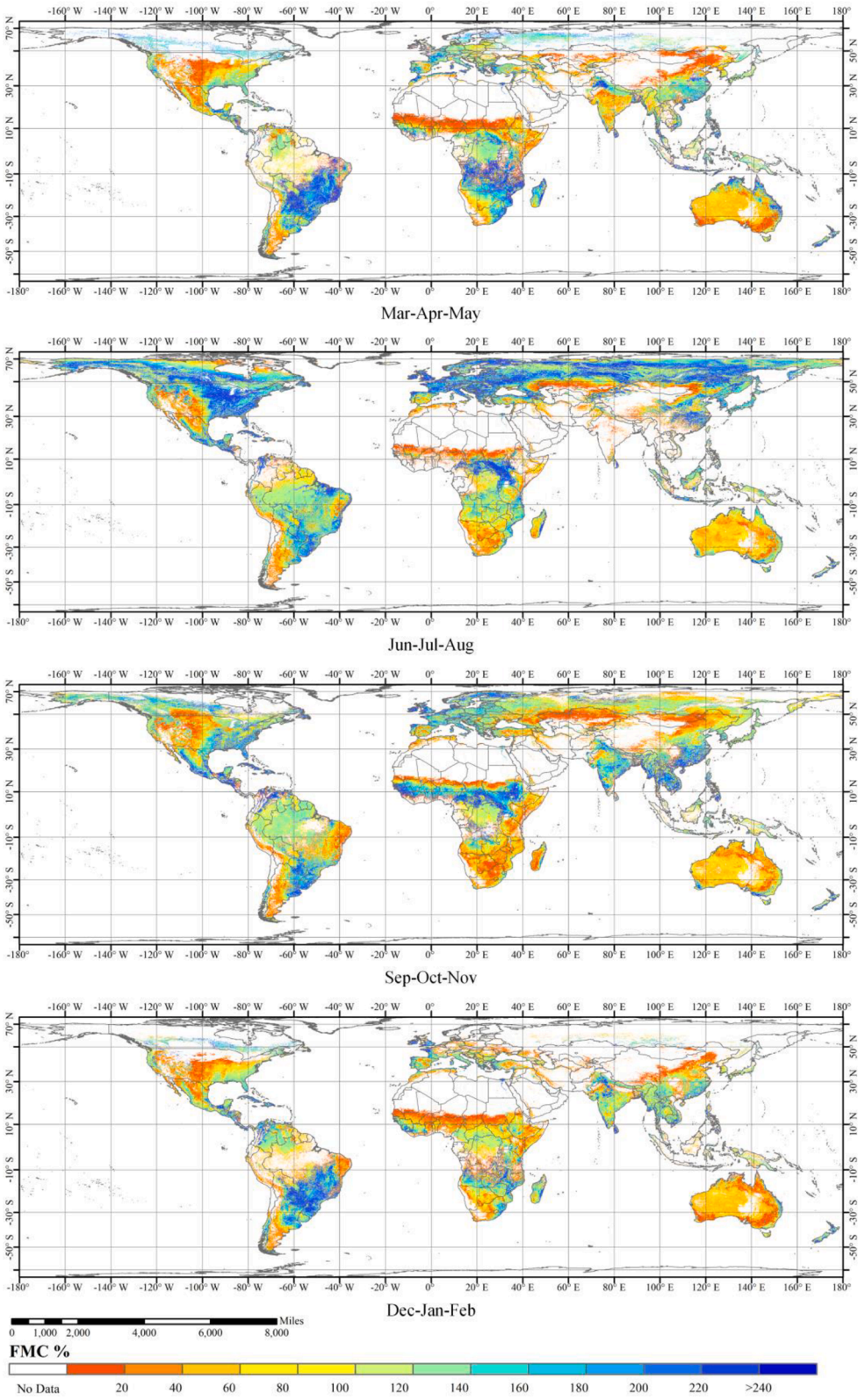

Fig. 7. Global median seasonal FMC spatial distribution at 500 m resolution in 2017–2018.

biased towards grassland (31.28%) and forest (49.87%) with substantially less shrubland samples (18.85%) (Table S2 & S3). The sampling sites were not evenly distributed across the globe to represent the main plant functional types (being tropical sites underrepresented) nor the different countries (overall more data collected in the USA), and data were collected throughout different seasons (Except for China and Senegal) but generally more during the hot dry season, which is more prone to wildfires.

Although a full comparison of performance is not possible given the difference in the samples used as ground truth, compared with two recent large scale FMC mapping studies from satellite data, the accuracies reported here are better than Yebra et al. (2018a) study for

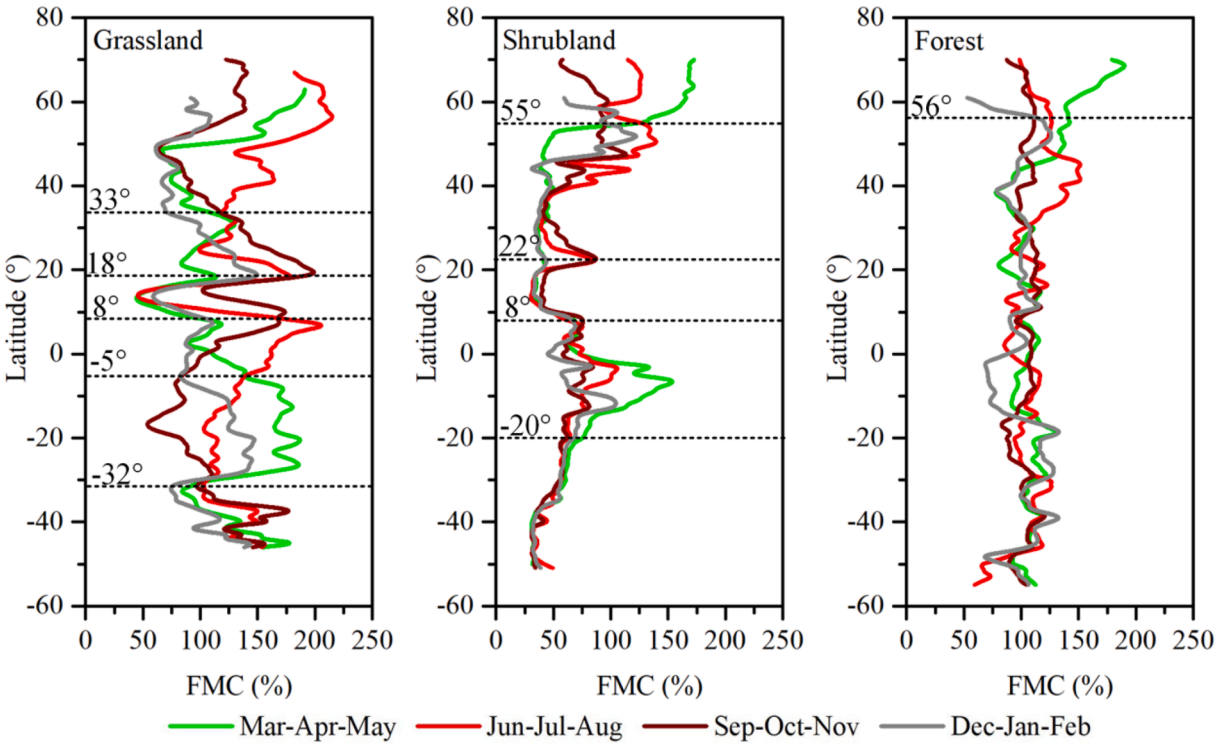

Fig. 8. Average global FMC for the four periods and three fuel classes between 2017 and 2018 calculated for different latitudes.

continental Australia with MODIS MCD43A4 Collection 5 reflectance data and RTM approaches (R^2 = 0.58 and RMSE = 40%) and slightly worse than Rao et al. (2020) accuracies reported for the western US with Sentinel 1 & Landsat 8 and a recurrent neural network model (R^2 = 0.63 and RMSE = 25%). In fact, the selection of optimal (R^2 = 0.71, RMSE = 32.36%, $p < 0.01$) and strict (R^2 = 0.69, RMSE = 34.05%, $p < 0.01$) filter rules, resulted in higher R^2 than that reported by Rao et al. (2020) considering the three fuel classes, but with a higher RMSE. Discriminated by fuel class, the optimal filter rule showed a higher R^2 (0.75) and RMSE (44.00%) than Rao et al. (2020)'s accuracy for grassland (R^2 = 0.56, RMSE = 31.00%), lower R^2 (0.59) and RMSE (22.09%) for shrubland (R^2 = 0.69, RMSE = 28.90%), and a slightly lower R^2 (0.45) and similar RMSE (21.53%) for forest (R^2 = 0.49 ~ 0.61, RMSE = 20.00%~27.7%). Finally, the advantage of this FMC product is its higher temporal resolution (daily) than Rao et al. (2020)'s product (15-day) and the larger scale (global). Consequently, the product presented in this study is better-suited for near-real-time monitoring of fuel flammability and ignition potential at a global scale.

The latest MODIS IGBP landcover product Collection 6 classified the grassland, shrubland, and forest classes by merging several of its original 17 classes that met the assumptions from specific RTMs and each fuel class had a specific LUT and inversion strategy. For example, regions like the Indian subcontinent and most of the cropland areas of eastern Brazil were classified as grasslands. However, this re-classification did not affect the retrieval of FMC because assumptions made by PROSAIL RTM (model used to generate the LUT for grasslands) resemble the conditions found in both cropland and grassland. Similarly, the savanna class was re-classified as forest rather than grassland class despite the low forest canopy coverage in this ecosystem. This re-classification was considered adequate because both forest and savannas are ecosystems composed of two layers of canopies and, therefore, their reflectance was modeled by coupling PROSAIL RTM (lower grassland canopy) and PROGeoSail RTM (overstory tree canopy).

Nevertheless, even if the MCD12Q1 Collection 6 algorithm highly outperformed Collection 5 (Sulla-Menashe et al., 2019), misclassification between classes with different LUTs and inversion strategies may still exist. This misclassification will propagate errors in the FMC computation given an incorrect LUT and inversion strategy, which will result in different retrieved FMC values. The potential improvements could be achieved by adding more fuel categories and using more complex RTMs, but this remains unknown given the lack of a validation data set with enough samples of fuel classes.

Grassland FMC presented the highest annual dynamics, in all latitudes followed by the shrubland and forest. However, the highest grassland FMC between 33°N to 18°N latitude occurred in the period of Sep-Oct-Nov rather than in Jun-Jul-Aug. This is partly because of the rainy season and high coverage of clouds in India and Southeast Asia in Jun-Jul-Aug (Fig. 7) and no data available in this period. Between the 22°N and 8°N, the sharp drop in grassland and shrubland FMC is mainly explained because of the low FMC values in areas of North Africa closed to the Sahara Desert (Fig. 7). The shrubland FMC did not change much between 20°S and 40°S latitude, given the low FMC values of vast dry central Australia (Fig. 7). Overall, the global FMC dynamics obtained were consistent with vegetation drought seasonal patterns (SPEI Global Drought Monitor. Available online: http://sac.csic.es/spei/index.html).

5.3. Future applications

Due to climate changes, the trend, frequency and burn severity of wildfires are increased and have already reached an alarming scale in many regions of the world, such as recent mega-fires in the western USA (2018), Amazon jungle (2019) and eastern Australia (2019–2020) (Argañaraz et al., 2015; Johnston et al., 2020; Littell et al., 2016; Moritz et al., 2012; Ward et al., 2020). Wildfire danger assessment is thus essential for wildfire early warning and management and is a critical part of fire prevention (Chuvieco et al., 2010). As a critical factor driving the fuel ignition and fire spread, the importance of FMC for wildfire danger assessment is evident in the different ecosystems in the world (Arganaraz et al., 2016; Chuvieco et al., 2004a; Dennison et al., 2008; Luo et al., 2019; Nolan et al., 2016; Yebra et al., 2018a). The produce developed here provides near-real-time, high temporal resolution (daily) and moderate spatial resolution (500 m) highly accurate (R^2 =

0.71, RMSE = 32.36%, $p < 0.01$) FMC estimates on a global scale. This dataset is encouraging for operational wildfire danger assessment. Since the FMC characterizes the status of water in vegetation, this product also has potential applications in monitoring drought and vegetation health and guiding forest cultivation.

Another dominant feature of this global FMC product is its generation from the RTMs inversion techniques. Empirical models require calibration only valid for a local region. The generalization power of RTMs makes them applicable to the global scale. This is important as most prior work to estimate FMC from remote sensing data was carried out and concentrated in Europe, the USA and Australia (Yebra et al., 2013). Other fire-prone regions such as the Amazon rain forest, Africa and East Asia lack such information.

Since the launch in 1999 (Terra) and 2002 (Aqua), MODIS has successfully operated for>18 years. However, the expected lifetime of the Terra and Aqua satellites has already been exceeded, and at some point, in the not-too-distant future, they will become inoperative. Yebra et al. (2018b) evaluated the feasibility and relative benefits of data sources including the geostationary Japanese Himawari-8 satellite (10 min, 2 km), the European Sentinel-2 (5 *days*, 20 m), the Landsat (16 *days*, 30 m) and Visible Infrared Imaging Radiometer Suite (VIIRS) (*daily*, 750 m) satellites for FMC retrieval in Australia. They reported a similar accuracy of these satellite data for FMC retrieval when applied the RTM-based methodology. Among them, the VIIRS obtained the highest accuracy retrieval, followed by Sentinel-2, Landsat-8 and Himawari-8. One possible explanation is that the VIIRS has five bands in the SWIR, which are key for water content estimation, followed by Sentinel-2 (3 bands), Landsat and Himawari-8 (two bands each). Therefore, the VIIRS is likely the best candidate to ensure data continuity. Currently, designed and built by the same instrument vendor as MODIS, two VIIRS instruments are operating in space, one on board the S-NPP satellite launched in October 2011 and another on the NOAA-20 satellite (formerly known as the JPSS-1) launched in November 2017 (Xiong and Butler, 2020). After compensating for the spectral response in RTM between sensors, this MODIS data-based FMC methodology can be therefore applied to the VIIRS data due to their similar spectral range, spatial resolutions, and calibration capability. This may enable the FMC product from VIIRS to be extended beyond 2040 (Xiong and Butler, 2020).

6. Conclusions

This study presented the first global FMC product based on RTMs and MODIS MCD43A4 reflectance data. The IGBP landcover type classified the vegetation into grassland, shrubland and forest fuel classes. For each fuel class, available prior information on model parameters carefully parameterized the RTMs, analyzing different inversion strategies. Selecting the VIs most sensitive to FMC variations obtained the optimal inversion strategy for each fuel class with EVI-NDVI-NDII-MSI-G_{ratio}, NDII-EVI-VARI-G_{ratio}, and NDII-EVI-GVMI-G_{ratio} for grassland, shrubland and forest, respectively. The cost functions were $RMSE_f$ for grassland and shrubland; and LAE for forest. The median value of the FMC values from 1% of the ranked $f(v,w)$ solutions rendered the final retrieved FMC. A large number of FMC measurements (3,034) from a global database assessed the accuracy of the FMC estimates. FMC estimates compared favorably to measurements when using a optimal rule to filter poor quality data ($R^2 = 0.71$, RMSE = 32.36%, $p < 0.01$). Preliminary analysis of FMC dynamics in 2017 and 2018 showed that FMC presents different patterns for different periods and latitudes. Overall, grassland FMC has the highest annual dynamics, followed by the shrubland and forest curves. Hence, this FMC product is encouraging for guiding future wildfire prevention, suppression, and response.

7. Author statement

All the authors have made substantial contributions, including those who provided editing and writing assistance.

Declaration of Competing Interest

The authors declare that they have no known competing financial interests or personal relationships that could have appeared to influence the work reported in this paper.

Acknowledgements

This work was supported by the National Natural Science Foundation of China (Contract No. 41801272 and U20A2090) and Sichuan Science and Technology Program (Contract No. 2020YFS0058). The authors are grateful to the Land Processes Distributed Active Archive Center (LPDAAC) at the U.S. Geological Survey (USGS) Earth Resources Observation and Science Center (EROS) (http://lpdaac.usgs.gov) for providing the MODIS dataset.

Appendix A. Supplementary data

Supplementary data to this article can be found online at https://doi.org/10.1016/j.jag.2021.102354.

References

Al-Moustafa, T., Armitage, R.P., Danson, F.M., 2012. Mapping fuel moisture content in upland vegetation using airborne hyperspectral imagery. Remote Sens Environ 127, 74–83.

Argañaraz, J.P., Gavier Pizarro, G., Zak, M., Landi, M.A., Bellis, L.M., 2015. Human and biophysical drivers of fires in Semiarid Chaco mountains of Central Argentina. Science of The Total Environment 520, 1–12.

Arganaraz, J.P., Landi, M.A., Bravo, S.J., Gavier-Pizarro, G.I., Scavuzzo, C.M., Bellis, L. M., 2016. Estimation of Live Fuel Moisture Content From MODIS Images for Fire Danger Assessment in Southern Gran Chaco. IEEE Journal of Selected Topics in Applied Earth Observations and Remote Sensing 9, 5339–5349.

Bicheron, P., Leroy, M., 1999. A method of biophysical parameter retrieval at global scale by inversion of a vegetation reflectance model. Remote Sens Environ 67, 251–266.

Bowyer, P., Danson, F.M., 2004. Sensitivity of spectral reflectance to variation in live fuel moisture content at leaf and canopy level. Remote Sens Environ 92, 297–308.

Caccamo, G., Chisholm, L.A., Bradstock, R.A., Puotinen, M.L., Pippen, B.G., 2012. Monitoring live fuel moisture content of heathland, shrubland and sclerophyll forest in south-eastern Australia using MODIS data. International Journal of Wildland Fire 21, 257.

Casas, A., Riaño, D., Ustin, S.L., Dennison, P., Salas, J., 2014. Estimation of water-related biochemical and biophysical vegetation properties using multitemporal airborne hyperspectral data and its comparison to MODIS spectral response. Remote Sens. Environ. 148, 28–41.

Ceccato, P., Flasse, S., Grégoire, J.-M., 2002. Designing a spectral index to estimate vegetation water content from remote sensing data. Remote Sens Environ 82, 198–207.

Cheng, T., Riaño, D., Ustin, S.L., 2014. Detecting diurnal and seasonal variation in canopy water content of nut tree orchards from airborne imaging spectroscopy data using continuous wavelet analysis. Remote Sens Environ 143, 39–53.

Cheng, Y.-B., Zarco-Tejada, P.J., Riaño, D., Rueda, C.A., Ustin, S.L., 2006. Estimating vegetation water content with hyperspectral data for different canopy scenarios: Relationships between AVIRIS and MODIS indexes. Remote Sensing of Environment 105, 354–366.

Chladil, M.A., Nunez, M., 1995. Assessing Grassland Moisture and Biomass in Tasmania - the Application of Remote-Sensing and Empirical-Models for a Cloudy Environment. International Journal of Wildland Fire 5, 165–171.

Chuvieco, E., Aguado, I., Cocero, D., Riaño, D., 2003. Design of an empirical index to estimate fuel moisture content from NOAA-AVHRR images in forest fire danger studies. International Journal of Remote Sensing 24, 1621–1637.

Chuvieco, E., Aguado, I., Dimitrakopoulos, A.P., 2004a. Conversion of fuel moisture content values to ignition potential for integrated fire danger assessment. Canadian Journal of Forest Research 34, 2284–2293.

Chuvieco, E., Aguado, I., Yebra, M., Nieto, H., Salas, J., Martín, M.P., Vilar, L., Martínez, J., Martín, S., Ibarra, P., de la Riva, J., Baeza, J., Rodríguez, F., Molina, J. R., Herrera, M.A., Zamora, R., 2010. Development of a framework for fire risk assessment using remote sensing and geographic information system technologies. Ecol Model 221, 46–58.

Chuvieco, E., Cocero, D., Riaño, D., Martin, P., Martínez-Vega, J., de la Riva, J., Pérez, F., 2004b. Combining NDVI and surface temperature for the estimation of live fuel moisture content in forest fire danger rating. Remote Sens Environ 92, 322-331.

Chuvieco, E., Riaño, D., Aguado, I., Cocero, D., 2002. Estimation of fuel moisture content from multitemporal analysis of Landsat Thematic Mapper reflectance data: Applications in fire danger assessment. Int. J. Remote Sens. 23, 2145–2162.

Combal, B., Baret, F., Weiss, M., Trubuil, A., Mace, D., Pragnere, A., Myneni, R., Knyazikhin, Y., Wang, L., 2003a. Retrieval of canopy biophysical variables from

bidirectional reflectance - Using prior information to solve the ill-posed inverse problem. Remote Sens Environ 84, 1–15.
Combal, B., Baret, F., Weiss, M., Trubuil, A., Mace, D., Pragnere, A., Myneni, R., Knyazikhin, Y., Wang, L., 2003b. Retrieval of canopy biophysical variables from bidirectional reflectance: Using prior information to solve the ill-posed inverse problem. Remote sensing of environment 84, 1–15.
Darvishzadeh, R., Skidmore, A., Schlerf, M., Atzberger, C., 2008. Inversion of a radiative transfer model for estimating vegetation LAI and chlorophyll in a heterogeneous grassland. Remote Sens Environ 112, 2592–2604.
Dawson, T.P., Curran, P.J., Plummer, S.E., 1998. LIBERTY - Modeling the effects of leaf biochemical concentration on reflectance spectra. Remote Sens Environ 65, 50–60.
De Santis, A., Chuvieco, E., Vaughan, P.J., 2009. Short-term assessment of burn severity using the inversion of PROSPECT and GeoSail models. Remote Sens. Environ. 113, 126–136.
Dennison, P.E., Moritz, M.A., Taylor, R.S., 2008. Evaluating predictive models of critical live fuel moisture in the Santa Monica Mountains, California. International Journal of Wildland Fire 17, 18–27.
Dennison, P.E., Roberts, D.A., Thorgusen, S.R., Regelbrugge, J.C., Weise, D., Lee, C., 2003. Modeling seasonal changes in live fuel moisture and equivalent water thickness using a cumulative water balance index. Remote Sens Environ 88, 442–452.
Fan, L., Wigneron, J.P., Xiao, Q., Al-Yaari, A., Wen, J., Martin-StPaul, N., Dupuy, J.L., Pimont, F., Al Bitar, A., Fernandez-Moran, R., Kerr, Y.H., 2018. Evaluation of microwave remote sensing for monitoring live fuel moisture content in the Mediterranean region. Remote Sens. Environ. 205, 210–223.
Fang, H., Liang, S., Kuusk, A., 2003. Retrieving leaf area index using a genetic algorithm with a canopy radiative transfer model. Remote sensing of environment 85, 257–270.
Feret, J.B., Francois, C., Asner, G.P., Gitelson, A.A., Martin, R.E., Bidel, L.P.R., Ustin, S.L., le Maire, G., Jacquemoud, S., 2008. PROSPECT-4 and 5: Advances in the leaf optical properties model separating photosynthetic pigments. Remote Sens Environ 112, 3030–3043.
Feret, J.B., Francois, C., Gitelson, A., Asner, G.P., Barry, K.M., Panigada, C., Richardson, A.D., Jacquemoud, S., 2011. Optimizing spectral indices and chemometric analysis of leaf chemical properties using radiative transfer modeling. Remote Sens Environ 115, 2742–2750.
García-Haro, F.J., Campos-Taberner, M., Moreno, Á., Tagesson, H.T., Camacho, F., Martínez, B., Sánchez, S., Piles, M., Camps-Valls, G., Yebra, M., Gilabert, M.A., 2020. A global canopy water content product from AVHRR/Metop. Isprs J Photogramm 162, 77–93.
García, M., Chuvieco, E., Nieto, H., Aguado, I., 2008. Combining AVHRR and meteorological data for estimating live fuel moisture content. Remote Sens Environ 112, 3618–3627.
García, M., Riaño, D., Yebra, M., Salas, J., Cardil, A., Monedero, S., Ramirez, J., Martín, M.P., Vilar, L., Gajardo, J., Ustin, S., 2020. A Live Fuel Moisture Content Product from Landsat TM Satellite Time Series for Implementation in Fire Behavior Models. Remote Sens-Basel 12, 1714.
Gorelick, N., Hancher, M., Dixon, M., Ilyushchenko, S., Thau, D., Moore, R., 2017. Google Earth Engine: Planetary-scale geospatial analysis for everyone. Remote Sens Environ 202.
Hao, X., Qu, J.J., 2007. Retrieval of real-time live fuel moisture content using MODIS measurements. Remote Sens Environ 108, 130–137.
Hosgood, B., Jacquemoud, S., Andreoli, G., Verdebout, J., Pedrini, G., Schmuck, G., 1995. Leaf optical properties experiment 93 (LOPEX93). Ispra Italy'European Commission, Joint Research Centre Institute of Remote Sensing Applications.
Houborg, R., Soegaard, H., Boegh, E., 2007. Combining vegetation index and model inversion methods for the extraction of key vegetation biophysical parameters using Terra and Aqua MODIS reflectance data. Remote Sens Environ 106, 39–58.
Huemmrich, K.F., 2001. The GeoSail model: a simple addition to the SAIL model to describe discontinuous canopy reflectance. Remote Sens Environ 75, 423–431.
Johnston, F.H., Borchers-Arriagada, N., Morgan, G.G., Jalaludin, B., Palmer, A.J., Williamson, G.J., Bowman, D.M., 2020. Unprecedented health costs of smoke-related PM 2.5 from the 2019–20 Australian megafires. Nature Sustainability 1–6.
Jolly, W.M., 2007. Sensitivity of a surface fire spread model and associated fire behaviour fuel models to changes in live fuel moisture. International Journal of Wildland Fire 16, 503.
Jurdao, S., Yebra, M., Guerschman, J.P., Chuvieco, E., 2013. Regional estimation of woodland moisture content by inverting Radiative Transfer Models. Remote Sens Environ 132, 59–70.
Kruse, F.A., Lefkoff, A.B., Boardman, J.W., Heidebrecht, K.B., Shapiro, A.T., Barloon, P. J., Goetz, A.F.H., 1993. The Spectral Image-Processing System (Sips) - Interactive Visualization and Analysis of Imaging Spectrometer Data. Remote Sens. Environ. 44, 145–163.
Kuusk, A., 1991. The Hot Spot Effect in Plant Canopy Reflectance. Springer, Berlin Heidelberg.
Leblon, B., Kasischke, E., Alexander, M., Doyle, M., Abbott, M., 2002. Fire danger monitoring using ERS-1 SAR images in the case of northern boreal forests. Natural Hazards 27, 231–255.
Leonenko, G., Los, S.O., North, P.R., 2013. Statistical distances and their applications to biophysical parameter estimation: Information measures, M-estimates, and minimum contrast methods. Remote Sens-Basel 5, 1355–1388.
Liao, Z., He, B., Quan, X., 2015. Modified enhanced vegetation index for reducing topographic effects. J Appl Remote Sens 9, 096068.
Littell, J.S., Peterson, D.L., Riley, K.L., Liu, Y., Luce, C.H., 2016. A review of the relationships between drought and forest fire in the United States. Global change biology 22, 2353–2369.
Luo, K., Quan, X., He, B., Yebra, M., 2019. Effects of Live Fuel Moisture Content on Wildfire Occurrence in Fire-Prone Regions over Southwest China. Forests 10, 887.
Lymburner, L., Tan, P., Mueller, N., Thackway, R., Thankappan, M., Islam, A., Lewis, A., Randall, L., Senarath, U., 2011. In: T.R.R. 2011/031 (Ed.), The National Dynamic Land Cover Dataset. .
Matsushita, B., Yang, W., Chen, J., Onda, Y., Qiu, G., 2007. Sensitivity of the Enhanced Vegetation Index (EVI) and Normalized Difference Vegetation Index (NDVI) to Topographic Effects: A Case Study in High-density Cypress Forest. Sensors (Basel) 7, 2636–2651.
Matthews, S., 2010. Effect of drying temperature on fuel moisture content measurements. International Journal of Wildland Fire 19, 800.
Meroni, M., Colombo, R., Panigada, C., 2004. Inversion of a radiative transfer model with hyperspectral observations for LAI mapping in poplar plantations. Remote Sens Environ 92, 195–206.
Moorthy, I., Miller, J.R., Noland, T.L., 2008. Estimating chlorophyll concentration in conifer needles with hyperspectral data: An assessment at the needle and canopy level. Remote Sens Environ 112, 2824–2838.
Moritz, M.A., Parisien, M.-A., Batllori, E., Krawchuk, M.A., Van Dorn, J., Ganz, D.J., Hayhoe, K., 2012. Climate change and disruptions to global fire activity. Ecosphere 3, 1–22.
Myneni, R.B., Hoffman, S., Knyazikhin, Y., Privette, J.L., Glassy, J., Tian, Y., Wang, Y., Song, X., Zhang, Y., Smith, G.R., Lotsch, A., Friedl, M., Morisette, J.T., Votava, P., Nemani, R.R., Running, S.W., 2002. Global products of vegetation leaf area and fraction absorbed PAR from year one of MODIS data. Remote Sens Environ 83, 214–231.
Neinavaz, E., Skidmore, A.K., Darvishzadeh, R., Groen, T.A., 2017. Retrieving vegetation canopy water content from hyperspectral thermal measurements. Agr Forest Meteorol 247, 365–375.
Nolan, R.H., Boer, M.M., Resco de Dios, V., Caccamo, G., Bradstock, R.A., 2016. Large-scale, dynamic transformations in fuel moisture drive wildfire activity across southeastern Australia. Geophys Res Lett 43, 4229–4238.
Paltridge, G.W., Barber, J., 1988. Monitoring grassland dryness and fire potential in australia with NOAA/AVHRR data. Remote Sensing of Environment 25, 381–394.
Peterson, S.H., Roberts, D.A., Dennison, P.E., 2008. Mapping live fuel moisture with MODIS data: A multiple regression approach. Remote Sens. Environ. 112, 4272–4284.
Pimont, F., Ruffault, J., Martin-StPaul, N.K., Dupuy, J.L., 2019. Why is the effect of live fuel moisture content on fire rate of spread underestimated in field experiments in shrublands? International Journal of Wildland Fire 28, 127.
Quan, X., He, B., Li, X., 2015. A Bayesian Network-Based Method to Alleviate the Ill-Posed Inverse Problem: A Case Study on Leaf Area Index and Canopy Water Content Retrieval. Ieee T Geosci Remote 53, 6507–6517.
Quan, X., He, B., Li, X., Liao, Z., 2016. Retrieval of Grassland Live Fuel Moisture Content by Parameterizing Radiative Transfer Model With Interval Estimated LAI. IEEE Journal of Selected Topics in Applied Earth Observations and Remote Sensing 9, 910–920.
Quan, X., He, B., Yebra, M., Yin, C., Liao, Z., Li, X., 2017a. Retrieval of forest fuel moisture content using a coupled radiative transfer model. Environ Modell Softw 95, 290–302.
Quan, X., Li, Y., He, B., Cary, G.J., Lai, G., 2021. Application of Landsat ETM+ and OLI Data for Foliage Fuel Load Monitoring Using Radiative Transfer Model and Machine Learning Method. IEEE Journal of Selected Topics in Applied Earth Observations and Remote Sensing, 1 1.
Quan, X.W., He, B.B., Yebra, M., Yin, C.M., Liao, Z.M., Zhang, X.T., Li, X., 2017b. A radiative transfer model-based method for the estimation of grassland aboveground biomass. Int. J. Appl. Earth Obs. 54, 159–168.
Rao, K., Williams, A.P., Flefil, J.F., Konings, A.G., 2020. SAR-enhanced mapping of live fuel moisture content. Remote Sens Environ 245, 111797.
Riaño, D., Vaughan, P., Chuvieco, E., Zarco-Tejada, P.J., Ustin, S.L., 2005. Estimation of fuel moisture content by inversion of radiative transfer models to simulate equivalent water thickness and dry matter content: analysis at leaf and canopy level. Ieee T Geosci Remote 43, 819–826.
Roberts, D., Dennison, P., Peterson, S., Sweeney, S., Rechel, J., 2006. Evaluation of Airborne Visible/Infrared Imaging Spectrometer (AVIRIS) and Moderate Resolution Imaging Spectrometer (MODIS) measures of live fuel moisture and fuel condition in a shrubland ecosystem in southern California. J Geophys Res-Biogeo 111.
Schlerf, M., Atzberger, C., 2006. Inversion of a forest reflectance model to estimate structural canopy variables from hyperspectral remote sensing data. Remote Sens Environ 100, 281–294.
Sulla-Menashe, D., Gray, J.M., Abercrombie, S.P., Friedl, M.A., 2019. Hierarchical mapping of annual global land cover 2001 to present: The MODIS Collection 6 Land Cover product. Remote Sens Environ 222, 183–194.
Tanase, M.A., Panciera, R., Lowell, K., Aponte, C., 2015. Monitoring live fuel moisture in semiarid environments using L-band radar data. International Journal of Wildland Fire 24, 560.
Trombetti, M., Riano, D., Rubio, M.A., Cheng, Y.B., Ustin, S.L., 2008. Multi-temporal vegetation canopy water content retrieval and interpretation using artificial neural networks for the continental USA. Remote Sens Environ 112, 203–215.
Verbesselt, J., Somers, B., Lhermitte, S., Jonckheere, I., Van Aardt, J., Coppin, P., 2007. Monitoring herbaceous fuel moisture content with SPOT VEGETATION time-series for fire risk prediction in savanna ecosystems. Remote Sens Environ 108, 357–368.
Verhoef, W., 1984. Light scattering by leaf layers with application to canopy reflectance modeling: The SAIL model. Remote Sens Environ 16, 125–141.
Verhoef, W., 1998. Theory of radiative transfer models applied in optical remote sensing of vegetation canopies. Prof.

Verhoef, W., Bach, H., 2007. Coupled soil–leaf-canopy and atmosphere radiative transfer modeling to simulate hyperspectral multi-angular surface reflectance and TOA radiance data. Remote Sens Environ 109, 166–182.
Verrelst, J., Rivera, J.P., Leonenko, G., Alonso, L., Moreno, J., 2013. Optimizing LUT-Based RTM Inversion for Semiautomatic Mapping of Crop Biophysical Parameters from Sentinel-2 and -3 Data: Role of Cost Functions. IEEE Transactions on Geoscience & Remote Sensing 52, 257–269.
Verrelst, J., Rivera, J.P., Leonenko, G., Alonso, L., Moreno, J., 2014. Optimizing LUT-based RTM inversion for semiautomatic mapping of crop biophysical parameters from Sentinel-2 and-3 data: Role of cost functions. Ieee T Geosci Remote 52, 257–269.
Verrelst, J., Rivera, J.P., Veroustraete, F., Muñoz-Marí, J., Clevers, J.G.P.W., Camps-Valls, G., Moreno, J., 2015. Experimental Sentinel-2 LAI estimation using parametric, non-parametric and physical retrieval methods – A comparison. Isprs J Photogramm 108, 260–272.
Wang, L., Hunt, E.R., Qu, J.J., Hao, X., Daughtry, C.S.T., 2013. Remote sensing of fuel moisture content from ratios of narrow-band vegetation water and dry-matter indices. Remote Sens Environ 129, 103–110.
Wang, L., Quan, X., He, B., Yebra, M., Xing, M., Liu, X., 2019. Assessment of the Dual Polarimetric Sentinel-1A Data for Forest Fuel Moisture Content Estimation. Remote Sens-Basel 11, 1568.
Ward, M., Tulloch, A.I., Radford, J.Q., Williams, B.A., Reside, A.E., Macdonald, S.L., Mayfield, H.J., Maron, M., Possingham, H.P., Vine, S.J., 2020. Impact of 2019–2020 mega-fires on Australian fauna habitat. Nature Ecology & Evolution 1–6.
Weise, D.R., Hartford, R.A., Mahaffey, L., 1998. Assessing live fuel moisture for fire management applications. Assessing Live Fuel Moisture For Fire Management Applications. Pages 49-55 in Teresa L. Pruden and Leonard A. Brennan (eds.).
Xiong, X., Butler, J.J., 2020. MODIS and VIIRS Calibration History and Future Outlook. Remote Sens-Basel 12, 2523.
Yebra, M., Chuvieco, E., 2009a. Generation of a Species-Specific Look-Up Table for Fuel Moisture Content Assessment. IEEE Journal of Selected Topics in Applied Earth Observations and Remote Sensing 2, 21–26.
Yebra, M., Chuvieco, E., 2009b. Linking ecological information and radiative transfer models to estimate fuel moisture content in the Mediterranean region of Spain: Solving the ill-posed inverse problem. Remote Sens Environ 113, 2403–2411.
Yebra, M., Chuvieco, E., Riaño, D., 2008. Estimation of live fuel moisture content from MODIS images for fire risk assessment. Agr Forest Meteorol 148, 523–536.
Yebra, M., Dennison, P.E., Chuvieco, E., Riaño, D., Zylstra, P., Hunt, E.R., Danson, F.M., Qi, Y., Jurdao, S., 2013. A global review of remote sensing of live fuel moisture content for fire danger assessment: Moving towards operational products. Remote Sens Environ 136, 455–468.
Yebra, M., Quan, X., Riaño, D., Rozas Larraondo, P., van Dijk, A.I.J.M., Cary, G.J., 2018a. A fuel moisture content and flammability monitoring methodology for continental Australia based on optical remote sensing. Remote Sens. Environ. 212, 260–272.
Yebra, M., Scortechini, G., Badi, A., Beget, M.E., Boer, M.M., Bradstock, R., Chuvieco, E., Danson, F.M., Dennison, P., Resco de Dios, V., Di Bella, C.M., Forsyth, G., Frost, P., Garcia, M., Hamdi, A., He, B., Jolly, M., Kraaij, T., Martin, M.P., Mouillot, F., Newnham, G., Nolan, R.H., Pellizzaro, G., Qi, Y., Quan, X., Riano, D., Roberts, D., Sow, M., Ustin, S., 2019. Globe-LFMC, a global plant water status database for vegetation ecophysiology and wildfire applications. Sci Data 6, 155.
Yebra, M., Dijk, A.v., Cary, G.J., 2018b. Evaluation of the feasibility and benefits of operational use of alternative satellite data in the Australian Flammability Monitoring System to ensure long-term data continuity. Bushfire and Natural Hazards CRC, Melbourne.
Youngentob, K.N., Zdenek, C., van Gorsel, E., Anderson, B., 2016. A simple and effective method to collect leaves and seeds from tall trees. Methods Ecol. Evol. 7, 1119–1123.
Zarco-Tejada, P.J., Berjon, A., Lopez-Lozano, R., Miller, J.R., Martin, P., Cachorro, V., Gonzalez, M.R., de Frutos, A., 2005. Assessing vineyard condition with hyperspectral indices: Leaf and canopy reflectance simulation in a row-structured discontinuous canopy. Remote Sens Environ 99, 271–287.
Zarco-Tejada, P.J., Miller, J.R., Harron, J., Hu, B.X., Noland, T.L., Goel, N., Mohammed, G.H., Sampson, P., 2004. Needle chlorophyll content estimation through model inversion using hyperspectral data from boreal conifer forest canopies. Remote Sens Environ 89, 189–199.